ORIGINAL ARTICLE

Structure-based drug discovery of novel fused-pyrazolone carboxamide derivatives as potent and selective AXL inhibitors

Feifei Fang[a,†], Yang Dai[b,†], Hao Wang[c,d], Yinchun Ji[b],
Xuewu Liang[b,d], Xia Peng[b], Jiyuan Li[b], Yangrong Zhao[b],
Chunpu Li[b,d], Danyi Wang[b,d], Yazhou Li[b], Dong Zhang[b],
Dan Zhang[b], Meiyu Geng[b,d,e,f], Hong Liu[b,d,f,*], Jing Ai[b,d,f,*],
Yu Zhou[c,d,f,*]

[a]Lingang Laboratory, Shanghai 200031, China
[b]State Key Laboratory of Drug Research, Shanghai Institute of Materia Medica, Chinese Academy of Sciences, Shanghai 201203, China
[c]Drug Discovery & Development Center, Shanghai Institute of Materia Medica, Chinese Academy of Sciences, Shanghai 201203, China
[d]University of Chinese Academy of Sciences, Beijing 100049, China
[e]Shandong Laboratory of Yantai Drug Discovery, Bohai Rim Advanced Research Institute for Drug Discovery, Yantai 264117, China
[f]School of Pharmaceutical Science and Technology, Hangzhou Institute for Advanced Study, UCAS, Hangzhou 310024, China

Abstract As a novel and promising antitumor target, AXL plays an important role in tumor growth, metastasis, immunosuppression and drug resistance of various malignancies, which has attracted extensive research interest in recent years. In this study, by employing the structure-based drug design and bioisosterism strategies, we designed and synthesized in total 54 novel AXL inhibitors featuring a fused-pyrazolone carboxamide scaffold, of which up to 20 compounds exhibited excellent AXL kinase and BaF3/TEL-AXL cell viability inhibitions. Notably, compound **59** showed a desirable AXL kinase inhibitory activity (IC$_{50}$: 3.5 nmol/L) as well as good kinase selectivity, and it effectively blocked the cellular

*Corresponding authors.
E-mail addresses: hliu@simm.ac.cn (Hong Liu), jai@simm.ac.cn (Jing Ai), zhouyu@simm.ac.cn (Yu Zhou).
†These authors made equal contributions to this work.

derivatives;
Antitumor drug
development

AXL signaling. In turn, compound **59** could potently inhibit BaF3/TEL-AXL cell viability (IC$_{50}$: 1.5 nmol/L) and significantly suppress GAS6/AXL-mediated cancer cell invasion, migration and wound healing at the nanomolar level. More importantly, compound **59** oral administration showed good pharmacokinetic profile and *in vivo* antitumor efficiency, in which we observed significant AXL phosphorylation suppression, and its antitumor efficacy at 20 mg/kg (qd) was comparable to that of BGB324 at 50 mg/kg (bid), the most advanced AXL inhibitor. Taken together, this work provided a valuable lead compound as a potential AXL inhibitor for the further antitumor drug development.

1. Introduction

AXL, a member of TAM (TYRO3, AXL and MER) subfamily of receptor tyrosine kinases (RTKs), is generally activated by binding to the endogenous ligand growth arrest specific protein 6 (GAS6), followed by self-dimerization and auto-phosphorylation[1]. The GAS6/AXL signaling could promote tumor progression through affecting multiple downstream signaling transduction including PI3K-AKT, STAT, RAS-RAF-MEK-ERK, and so on (Supporting Information Fig. S1)[2,3]. Moreover, AXL-RTKs could cross-talk to rewire the kinase signaling nodes in various malignancies[4]. GAS6/AXL axis is involved in multiple biological process of tumorigenesis and progression[2,5−9], such as tumor cell survival, motility, invasion and epithelial−mesenchymal transition (EMT). In particular, AXL is required for multiple steps of the metastasis cascade, thus blockage of AXL could decrease tumor metastasis[10−14]. Aberrant AXL signaling has also been found in several types of cancers and associated with high tumor recurrence and poor prognosis[15−19]. Accumulating evidences have highlighted the importance of GAS6/AXL axis in the tumor microenvironment (Fig. S1)[20−22], where it regulates the expression of major histocompatibility complex I (MHC-I) and programmed death ligand-1 (PD-L1), as well as promotes secretion of immunosuppressive chemokines[23−25]. Besides, GAS6/AXL signaling promotes infiltration of macrophages, monocytes and myeloid-derived suppressor cells (MDSCs), but reduces infiltration of CD4$^+$, CD8$^+$ T-cells and conventional dendritic cells (DC) in the tumor[21,26]. Furthermore, AXL high expression could cause innate as well as acquired resistance to anticancer therapies[27−30]. In short, AXL is a promising anticancer therapeutic target since it plays an important role in promoting tumorigenesis and immunosuppressive microenvironment as well as mediating drug resistance.

Currently available small-molecule AXL inhibitors are mainly classified into U-shaped type I and linear type II ATP-competitive inhibitors based on their structure characteristics and binding modes with AXL kinase (Fig. 1)[31−33]. BGB324 (**1**) also called Bemcentinib, was considered as the first type I selective AXL inhibitor with an IC$_{50}$ of 14 nmol/L[34], and its monotherapy and combination therapies have currently entered phase II clinical trials for several cancers including NSCLC and AML with positive clinical benefits[35−38]. Cabozantinib (**2**) represents a classic type II kinase inhibitor, which can occupy the additional allosteric pocket of kinase formed by the aspartate-phenylalanine-glycine motif far away from the active site (DFG-out), and was approved for the therapy of MTC, renal cell carcinoma and hepatocellular carcinoma[39]. However, Cabozantinib is not a selective AXL inhibitor, and it has very strong inhibitory activities against multiple kinases including VEGFR2, c-Met, KIT, FLT3, etc., which may lead to some potential toxicities and side effects. Some similar derivatives, such as BMS-777607 (**3**)[40], compounds **4−6**[41−43] and other reported AXL inhibitors[31,32,44−50], have been in different stages of preclinical and clinical trials for various cancer indications.
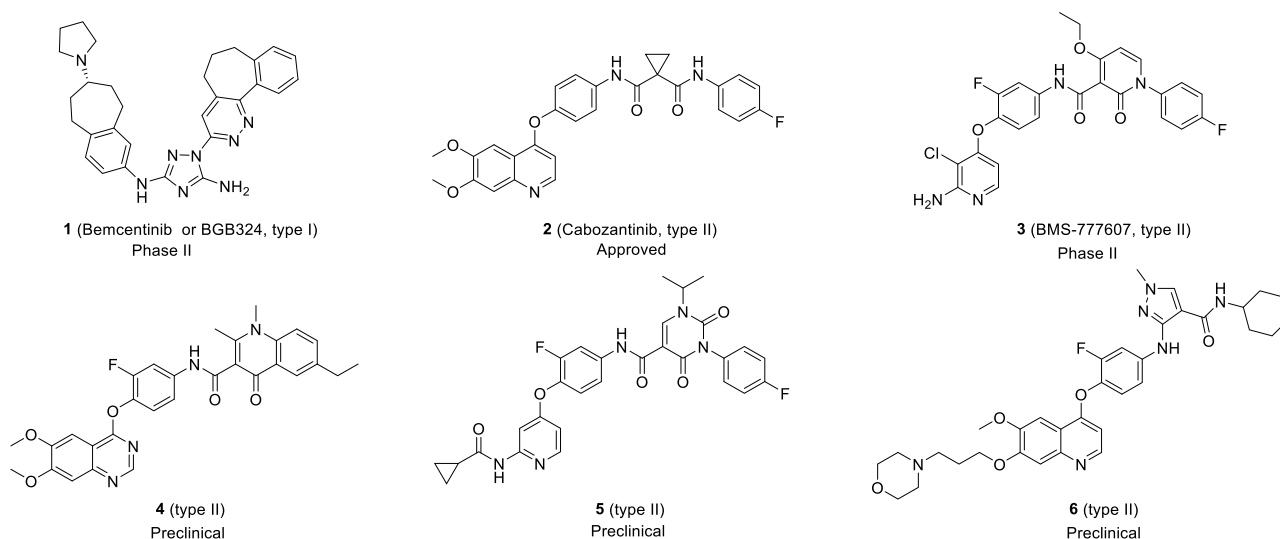
Figure 1 Chemical structures of reported representative AXL inhibitors.

In view of the importance of AXL in tumorigenesis and progression, the development of selective AXL inhibitors is of great significance for the clinical treatment of tumors.

Although AXL inhibitors could be a promising and powerful approach for various malignancies including solid tumors and hematological malignancies, the development of selective AXL inhibitors as anticancer agents still remains a great challenge. In this work, we have developed a novel class of selective AXL inhibitors featuring a fused-pyrazolone carboxamide scaffold, and demonstrated that most of them had more excellent AXL inhibitory activities and antitumor efficiencies than the most advanced selective AXL inhibitor BGB324.

2. Results and discussion

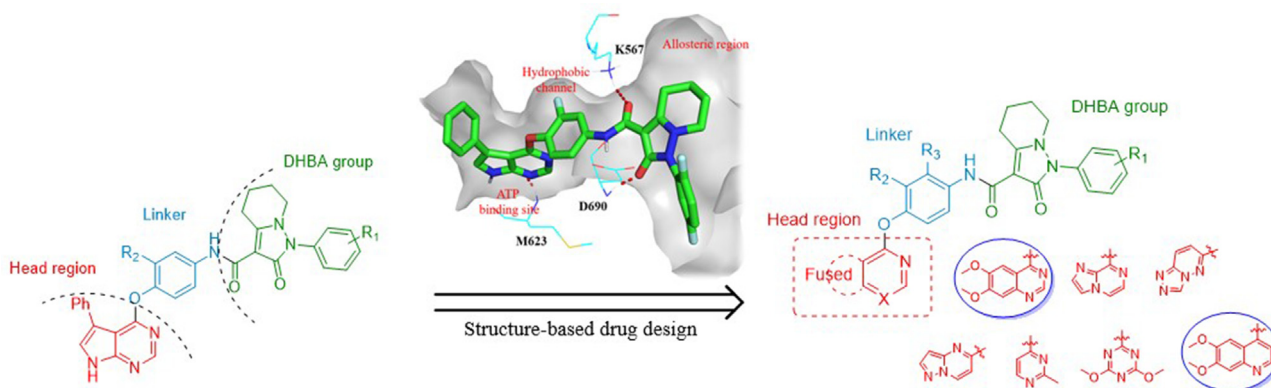### 2.1. Rational design of novel AXL inhibitors

Considering the significant therapeutic values of AXL inhibitors in overcoming drug resistance, tumor metastasis and immunosuppression, we first conducted a thoroughly biological screening of our in-house compound library to discover a new class of AXL inhibitors with a novel scaffold for hit-to-lead development. Fortunately, three fused-pyrazolone carboxamide derivatives 7−9 displayed acceptable inhibitory activities against AXL kinase, especially the inhibition rate of compound 9 reached 75.4 % at 100 nmol/L. More importantly, compound 9 displayed a relative

high selectivity against AXL in the kinase screening at 500 nmol/L, suggesting that compound 9 could be a novel hit compound for further modification (Fig. 2).

To find more potent AXL inhibitors, we adopted structure-based drug design and bioisosterism strategies to guide the structure design of compounds. We firstly performed the molecular docking analysis of compound 9 in the AXL DFG-out homology model (constructed with PDB ID: 7AAY and chain B of PDB ID: 7AVX as the templates) (Fig. 3). The results showed that the dual carbonyl motif of the fused-pyrazolone carboxamide in the DHBA (dual hydrogen bond acceptor) group formed two hydrogen bonds with K567 and D690 located in the allosteric pocket of AXL kinase, respectively, and its fused-piperidine ring occupied the allosteric cavity relatively well, which were speculated to be the key to the activity and selectivity of AXL inhibitors. In addition, the pyrrolo [2,3-d]pyrimidine in the head region of compound 9 could form a hydrogen bond with M623 located in the ATP binding region, enhancing the interaction between compound 9 and AXL kinase. The linker occupied the hydrophobic channel, which perfectly connected the DHBA moiety and head region. As the fused-pyrazolone carboxamide structure in the DHBA group is particularly important for the biological activity and selectivity, we retained this scaffold in the design of target compounds. Based on the above molecular docking analysis, we rationally carried out structural modifications on the head region using different aromatic heterocyclic rings, the linker and the phenyl in the DHBA moiety.

Compd.	R₁	R₂	AXL inhibition rate @ 100 nmol/L
7	H	H	31.6%
8	H	F	66.5%
9	2,5-di-F	F	75.4%
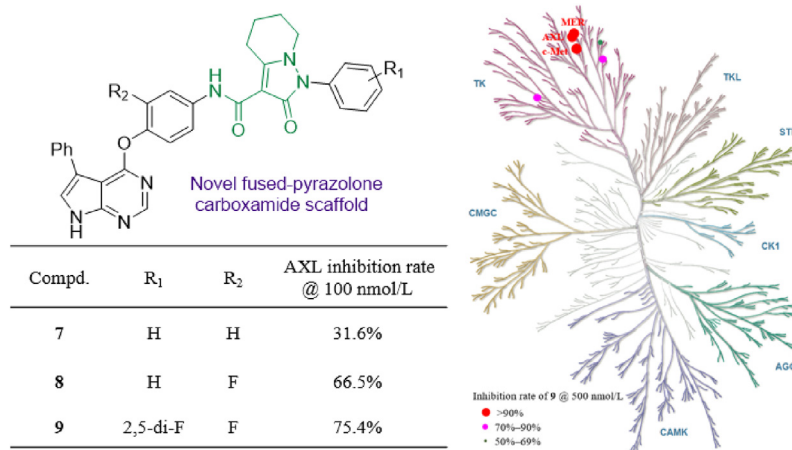
Figure 2   Discovery of selective AXL inhibitors featuring a novel fused-pyrazolone carboxamide scaffold.

Figure 3   Rational design of novel selective AXL inhibitors by employing the structure-based drug design and bioisosterism strategies.
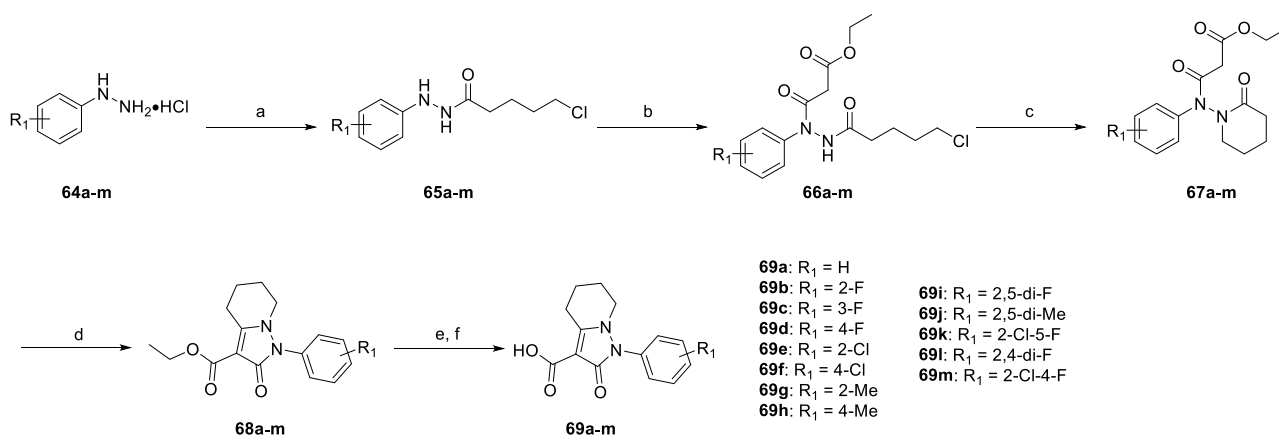
Scheme 1 Synthesis of key acid fragments **69a−m**. Reagents and conditions: (a) 5-Chloropentanoyl chloride, 10% Na$_2$CO$_3$ (aq), DCM, 0 °C−rt, overnight, 29%−58%; (b) Ethyl 3-chloro-3-oxopropanoate, Na$_2$CO$_3$, DCM, rt, overnight, 56%−80%; (c) NaH, DMF, 0 °C−rt, 5 h, 83%−90%; (d) DBU, 50 °C, 5 h, 85%−90%; (e) 2 N KOH (aq), EtOH, reflux, 1 h; (f) 2 N HCl (aq), rt, 0.5 h, 61%−79%.

Lead optimization was initiated with the head region, which was firstly explored by introducing diversified fused or single nitrogen-containing heterocycles (**10−15**) to form more appropriated interactions with the residues of AXL kinase hinge region. Then, single or double substituents were introduced into the phenyl ring of the DHBA moiety to investigate the hydrophobic interaction between different substituted benzene rings and the allosteric pocket (**16−28**). After that, different linkers connecting the head region and DHBA moiety were investigated to design compounds **29−55**. In the end, given the fact that quinoline rings often serve as adenine analogs to competitively bind to the hinge region of kinases, we further selected 6,7-dimethoxyquinoline as the head region and designed compounds **56−63**.

### 2.2. Synthesis of novel AXL inhibitors

Generally, all target compounds were prepared by a condensation of acid fragments **69a−m** and the corresponding amine fragments **74a−b**, **80a−o**, **82** and **85**.

The synthesis of key acid fragments **69a−m** were described in Scheme 1[51]. The free substituted phenylhydrazines, released from their hydrochlorides **64a−m** under Na$_2$CO$_3$ aqueous solution, were condensed with 5-chloropentanoyl chloride to form intermediates **65a−m**, followed by another condensation with ethyl 3-chloro-3-oxopropanoate to afford **66a−m**. Next, they were sequentially treated by sodium hydride (NaH) and 1,8-diazabicyclo [5.4.0] undec-7-ene (DBU) in the subsequent intramolecular nucleophilic substitution and aldol condensation to provide the corresponding ester derivatives **68a−m**, which were hydrolyzed to conveniently generate the fused-pyrazolone acid fragments **69a−m**.

Compounds **7−9** were synthesized according to the procedures outlined in Scheme 2. Commercially available 4-chloro-5-iodo-7H-pyrrolo [2,3-d]pyrimidine **70** was firstly protected with (2-(chloromethoxy)ethyl)trimethylsilane (SEMCl) to afford the intermediate **71**, which subsequently underwent a Suzuki coupling with phenylboronic acid, an intermolecular nucleophilic substitution with 4-nitrophenol or 2-fluoro-4-nitrophenol, and a nitro reduction to give the amine fragments **74a−b**, followed by a
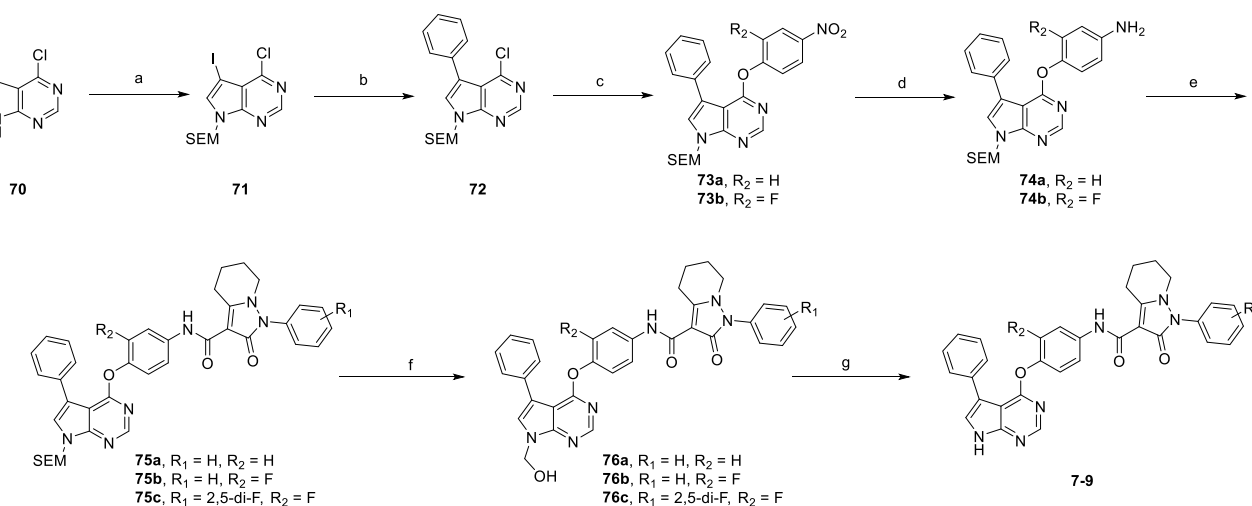
Scheme 2 Synthesis of compounds **7−9**. Reagents and conditions: (a) SEMCl, NaH, DMF, 0 °C−rt, overnight, 80%; (b) Phenylboric acid, Pd(PPh$_3$)$_4$, Na$_2$CO$_3$, H$_2$O, toluene, Ar, 90 °C, overnight, 71%; (c) 4-Nitrophenol or 2-fluoro-4-nitrophenol, PhCl, 140 °C, 8 h, 56%−59%; (d) NiCl$_2$·6H$_2$O, NaBH$_4$, THF/MeOH (3:1, v/v), 0 °C−rt, 2 h, 64%−66%; (e) **69a** or **69i**, HATU, DIPEA, DCM, rt, overnight, 69%−75%; (f) TFA, DCM, rt, overnight, 82%−86%; (g) NaOH, THF/H$_2$O (5/4, v/v), rt, overnight, 75%−79%.
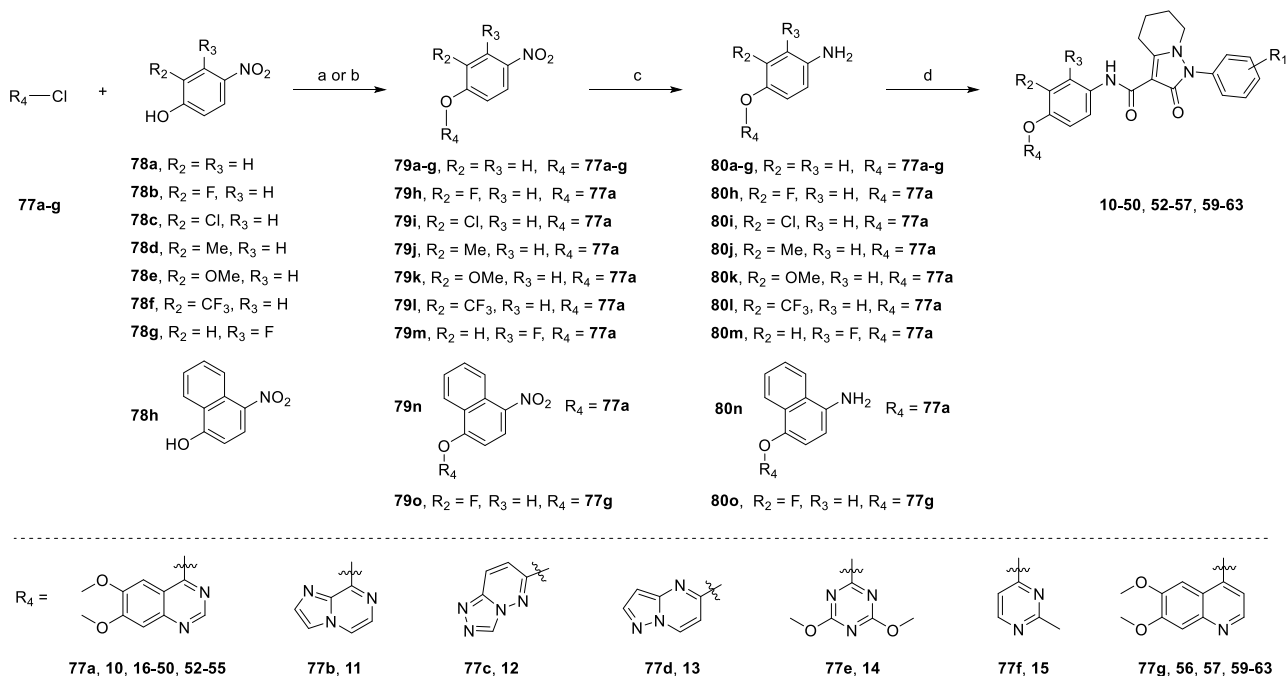
Scheme 3 Synthesis of compounds **10−50**, **52−57** and **59−63**. Reagents and conditions: (a) K_2CO_3, DMF, 85 °C, overnight, 58%−73%; (b) PhCl, 140 °C, 8 h, 52%−63%; (c) Fe/NH_4Cl, EtOH/H_2O (1:1, *v/v*), 75 °C, 1 h, 65%−79%; (d) **69a−m**, HATU, DIPEA, DCM, rt, overnight, 80%−90%.

condensation with **69a** or **69i**, and a two-step deprotection to generate the target compounds **7−9**, respectively.

The synthetic routes of target compounds **10−50**, **52−57** and **59−63** were summarized in Scheme 3. The chlorinated heterocyclic raw materials **77a−g** proceeded with substituted 4-nitrophenols **78a−g** (H, 2-F, 2-Cl, 2-Me, 2-OMe, 2-CF_3 and 3-F) or 4-nitronaphthalen-1-ol **78h** to give nitro intermediates **79a−o**, which were further transformed into the corresponding amine fragments **80a−o** under the Fe/NH_4Cl condition. Finally, these amine fragments were separately condensed with **69a−m** to yield the ultimate compounds **10−50**, **52−57** and **59−63**.

As shown in Scheme 4, the amine fragment **82** was smoothly obtained by treating 4-chloro-6,7-dimethoxyquinazoline **77a** with

tert-butyl (5-hydroxypyridin-2-yl)carbamate **81**, and underwent a subsequent condensation reaction with **69a** to yield the ultimate compound **51**. Moreover, 6,7-dimethoxyquinolin-4-ol **83** proceeded with 2-fluoro-5-nitropyridine to offer a nitro intermediate **84**, which was reduced and subsequently condensed with **69a** to offer the desired compound **58**.

2.3. Structure−activity relationship (SAR) exploration and their anticancer activities in vitro

The inhibitory activities of all compounds against AXL kinase were determined using an enzyme-linked immunosorbent assay (ELISA), and BGB324 (**1**), the most advanced (in clinical Phase II) selective
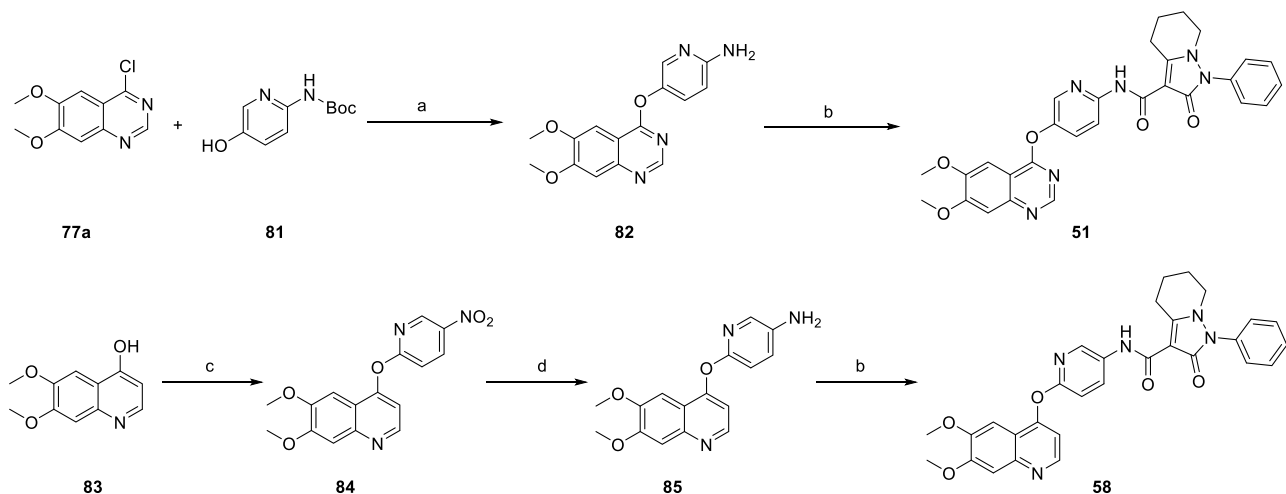
Scheme 4 Synthesis of compounds **51** and **58**. Reagents and conditions: (a) PhCl, 140 °C, 8 h, 39%; (b) **69a**, HATU, DIPEA, DCM, rt, overnight, 85%−88%; (c) 2-Fluoro-5-nitropyridine, Cs_2CO_3, DMF, 0 °C−rt, 2−3 h, 46%; (d) Fe/NH_4Cl, EtOH/H_2O (1:1, *v/v*), 75 °C, 1 h, 75%.

Table 1 Structures of compounds **10−28** and their inhibitory activities against AXL kinase and BaF3/TEL-AXL cell viability[a].
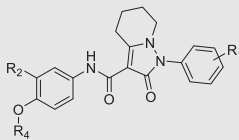
Compd.	R_1	R_2	R_4	IC$_{50}$ (nmol/L)[b] or inhibition rate[c]	
				AXL kinase	Cell viability[d]
10	H	H		43.9 ± 4.7	−
11	H	H		−9.5 %	−
12	H	H		−17.7 %	−
13	H	H		−18.9 %	−
14	H	H		−6.0 %	−
15	H	H		6.3 %	−
16	H	F		8.1 ± 0.2	<0.1
17	2-F	F		9.4 ± 3.2	<0.1
18	3-F	F		5.9 ± 0.6	<0.1
19	4-F	F		7.8 ± 1.1	<0.1
20	2-Cl	F		10.5 ± 0.5	7.0 ± 4.2
21	4-Cl	F		42.6 ± 6.2	−
22	2-Me	F		15.7 ± 1.7	7.6 ± 4.1
23	4-Me	F		27.3 ± 2.6	−
24	2,5-di-F	F		5.5 ± 1.6	<0.1
25	2,5-di-Me	F		78.4 ± 2.1	−
26	2-Cl-5-F	F		13.7 ± 3.1	5.2 ± 4.1
27	2,4-di-F	F		25.1 ± 1.6	−
28	2-Cl-4-F	F		13.5 ± 1.8	4.4 ± 2.2
BGB324 (**1**)				7.7 ± 2.9	95.1 ± 3.7

[a]All data were obtained as mean values from two independent experiments.
[b]The IC$_{50}$ values were represented as mean ± SD.
[c]The inhibition rate was determined at a concentration of 100 nmol/L.
[d]Cell viability inhibition was tested in BaF3/TEL-AXL cells, "−" means not evaluated.

Table 2 Structures of compounds **29–63** and their inhibitory activities against AXL kinase and BaF3/TEL-AXL cell viability[a].

Compd.	X	Linker	R₁	IC₅₀ (nmol/L)[b] or inhibition rate[c]	
				AXL kinase	Cell viability[d]
29	N		H	10.0 ± 1.4	2.3 ± 0.4
30	N		2-F	13.4 ± 0.8	<0.1
31	N		4-F	30.5 ± 4.9	–
32	N		2,5-di-F	37.0 ± 1.4	–
33	N		H	16.9 ± 2.5	1651.3 ± 443.7
34	N		2-F	30.9 ± 1.4	–
35	N		4-F	19.6 ± 1.9	–
36	N		2,5-di-F	6.6 ± 2.9	3632.1 ± 493.6
37	N		H	23.2 %	–
38	N		2-F	32.3 %	–
39	N		4-F	15.6 %	–
40	N		2,5-di-F	35.7 %	–
41	N		H	56.4 %	–
42	N		2-F	28.0 %	–
43	N		4-F	19.9 %	–
44	N		2,5-di-F	59.6 %	–
45	N		H	59.4 %	–
46	N		2-F	50.4 %	–
47	N		4-F	51.9 %	–
48	N		2,5-di-F	62.4 %	–
49	N		2-F	47.9 %	–
50	N		2,5-di-F	9.1 ± 0.2	7.8 ± 0.7
51	N		H	16.8 ± 3.5	3.3 ± 1.4

Table 2 (*continued*)

Compd.	X	Linker	R_1	IC$_{50}$ (nmol/L)[b] or inhibition rate[c]	
				AXL kinase	Cell viability[d]
52	N		H	41.0 %	—
53	N		2-F	41.4 %	—
54	N		4-F	39.0 %	—
55	N		2,5-di-F	50.4 %	—
56	CH		H	4.0 ± 0.4	1.0 ± 0.2
57	CH		H	2.5 ± 0.3	<0.1
58	CH		H	50.9 %	—
59	CH		4-F	3.5 ± 0.8	1.5 ± 0.4
60	CH		2,5-di-F	1.2 ± 0.5	<0.2
61	CH		2-Cl-5-F	0.7 ± 0.1	<0.2
62	CH		2,4-di-F	6.1 ± 0.8	0.7 ± 0.3
63	CH		2-Cl-4-F	2.3 ± 0.2	<0.2
BGB324 (**1**)				7.7 ± 2.9	95.1 ± 3.7

[a]All data were obtained as mean values from two independent experiments.
[b]The IC$_{50}$ values were represented as mean ± SD.
[c]The inhibition rate was determined at a concentration of 100 nmol/L.
[d]Cell viability inhibition was tested in BaF3/TEL-AXL cells, "—" means not evaluated.

AXL inhibitor, served as the positive control. All results were summarized in Table 1 and Table 2. Firstly, in the hope of forming more appropriate interactions with the hinge region of AXL kinase, we introduced diversified heterocyclic fragments at the head region, and obtained compounds **10−15**. The results shown in Table 1 revealed that compound **10** containing a quinazoline fragment showed the most potent AXL kinase inhibitory activity with an IC$_{50}$ value of 43.9 nmol/L, however, other fused heterocycles (**11−13**) or single heterocycles (**14** and **15**) as the head region all resulted in great loss of activities against AXL kinase, suggesting that quinazoline fragment was the most appropriate head region to enhance the AXL kinase inhibitory activity. Therefore, we kept quinazoline fragment in the head region, and modified the linker and DHBA group to synthesize compounds **16−28**.

Encouragingly, compound **16** with 2-fluoro-4-aminophenol as the linker had a more excellent inhibitory potency against AXL kinase
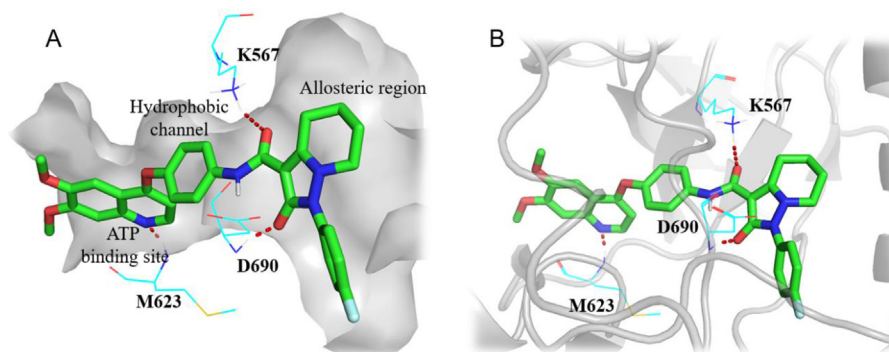
Figure 4 The binding mode of **59** (green) with the AXL DFG-out homology model (generated from PDB ID: 7AAY and chain B of PDB ID:7AVX). Hydrogen bonds were indicated by red dashed lines.
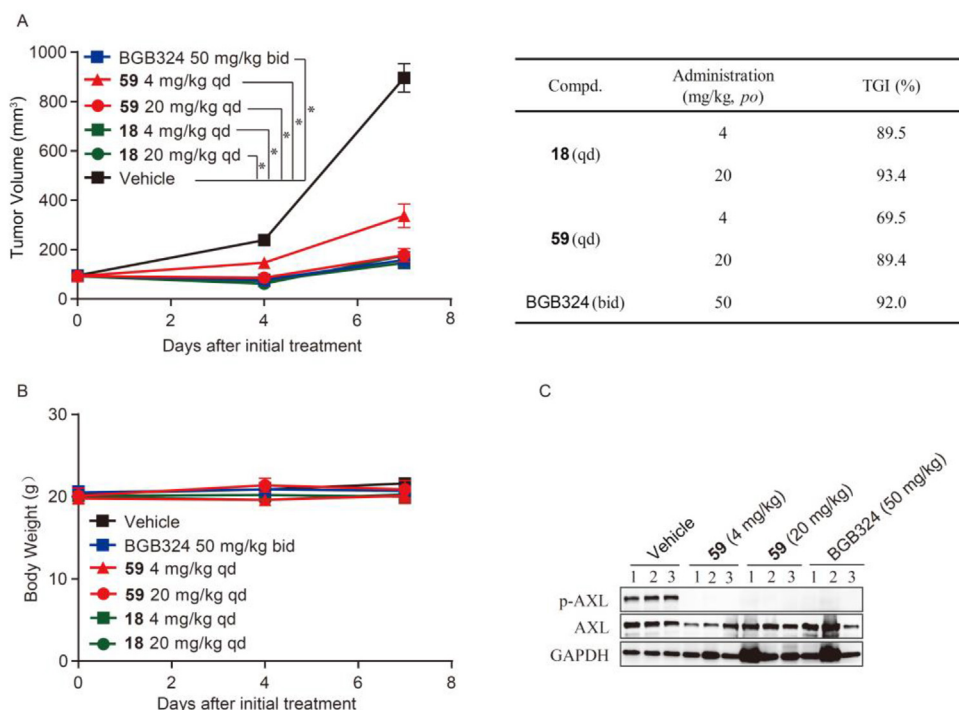
Table 3 Pharmacokinetic parameters of compounds **18**, **24** and **59** in mice[a].

Compd.	Admini.	T_{max}	C_{max}	AUC_{0-t}	$AUC_{0-\infty}$	$t_{1/2}$	CL	F
		(h)	(ng/mL)	(ng·h/mL)	(ng·h/mL)	(h)	(mL/min/kg)	(%)
18	*po*	2.0	2970	15,903	16,007	3.24	/	22.9
	iv	/	/	34,754	42,066	10.40	2.05	
24	*po*	2.0	1490	13,500	14,200	6.77	/	13.8
	iv	/	/	48,900	49,100	3.38	1.70	
59	*po*	1.0	2300	14,800	14,900	2.94	/	36.1
	iv	/	/	20,500	21,600	1.67	3.86	

[a]All data for each group were obtained as mean values from three animals. *po* at dose of 10 mg/kg iv at dose of 5 mg/kg.

with an IC_{50} value of 8.1 nmol/L. Meanwhile, compound **16** strongly inhibited the BaF3/TEL-AXL cell viability ($IC_{50} < 0.1$ nmol/L). Therefore, we further investigated the hydrophobic effects of different substituted benzene rings at R_1 position. Introduction of a single F atom at the *ortho*, *meta*, and *para* positions of the benzene ring alone (**17**−**19**) resulted in the similar AXL kinase inhibitions ($IC_{50} < 10$ nmol/L), and compound **18** possessed the strongest AXL kinase inhibition with an IC_{50} value of 5.9 nmol/L. It is worth mentioning that compounds **16**−**19** possessed very strong anti-BaF3/TEL-AXL cell viability potencies with their $IC_{50} < 0.1$ nmol/L. We further explored Cl and Me substituents at R_1 position, and found that the activities of *ortho*-substituted compounds **20** and **22** were superior to that of **21** and **23** substituted at *para*-position of the benzene ring (**20** IC_{50}: 10.5 nmol/L *vs* **21** IC_{50}: 42.6 nmol/L), respectively. Besides, compounds **24**−**28** with double substituents on the benzene ring also showed desirable AXL kinase inhibitions with IC_{50} ranging from 5.5 to 78.4 nmol/L.

Given the positive effects of 2-fluoro-4-aminophenol linker, we continued to explore the effects of the position of F atom in the linker and its bioisosteric groups such as Cl, Me, OMe, CF_3 groups on AXL kinase inhibitory activity. The results in Table 2 revealed that changing the position of F atom maintained the potent AXL inhibitory activities of compounds **29**−**32** with IC_{50} ranging from 10.0 to 37.0 nmol/L. Then, among compounds **33**−**36** featuring a 2-chloro-4-aminophenol linker, the IC_{50} value of **36** (2,5-di-F for R_1) reached 6.6 nmol/L. However, when introducing Me, OMe or CF_3 substituted 4-aminophenol as the linker, the corresponding compounds **37**−**48** showed poor inhibitory activities against AXL kinase at a concentration of 100 nmol/L, as did for **52**−**55** with a 4-nitronaphthalen-1-ol linker, which may be attributed to that the flat and slender hydrophobic channel was not enough to accommodate these larger substituents. Moreover, when 4-aminophenol was used as a linker, only compound **50** bearing 2,5-di-F substituents at the benzene ring of the DHBA moiety showed a significant AXL kinase inhibition (IC_{50}:

Compd.	Administration (mg/kg, *po*)	TGI (%)
18 (qd)	4	89.5
	20	93.4
59 (qd)	4	69.5
	20	89.4
BGB324 (bid)	50	92.0

Figure 5 Compounds **18** and **59** significantly inhibited tumor growth in BaF3/TEL-AXL mouse xenograft model. (A, B) Tumor volume (A) and body weight (B) changes during the treatment period. The data were expressed as the mean ± SEM. Significant differences from the vehicle group were determined using student's *t*-test analysis, *$P < 0.05$. (C) Compound **59** inhibited intratumoral AXL phosphorylation of subcutaneous BaF3/TEL-AXL tumor tissues. Subcutaneous BaF3/TEL-AXL tumor tissues were obtained 1 h after the last dosage. Then, intratumoral AXL phosphorylation level was determined by immunoblotting analysis.

9.1 nmol/L). Notably, the 6-aminopyridin-3-ol, as in **51** with an IC_{50} value of 16.8 nmol/L, could also be regarded as a potential linker.

It is well known that quinoline and its analogs could be bioisosteric groups of quinazoline, and they are a class of privileged scaffolds in many anticancer active compounds and drugs[52−59]. Therefore, we designed and synthesized compounds **56−63** by replacing 6,7-dimethoxyquinazoline with 6,7-dimethoxyquinoline as the head region to explore their effects on AXL inhibitory activity. It revealed that compounds **56** and **57** with 4-aminophenol and 2-fluoro-4-aminophenol linkers, respectively, displayed excellent and comparable biological activities (**56** IC_{50}: 4.0 nmol/L and **57** IC_{50}: 2.5 nmol/L), which were far superior to that of compound **58** with a 5-aminopyridin-2-ol linker. Based on these results, we further fixed R_1 as the 4-F substituent and synthesized compound **59**, which also significantly blocked AXL kinase with an IC_{50} value of 3.5 nmol/L. Meanwhile, compound **59** showed a potent BaF3/TEL-AXL cell viability inhibition with an IC_{50} value of 1.5 nmol/L. Besides, we further introduced double halogen substituents, such as 2,5-di-F (**60**), 2-Cl-5-F (**61**), 2,4-di-F (**62**) and 2-Cl-4-F (**63**), to R_1 position and demonstrated their excellent *in vitro* inhibitory effects against AXL with IC_{50} values less than 10 nmol/L. Overall, 6,7-dimethoxyquinoline was demonstrated to be beneficial for the activities of these AXL inhibitors. In summary, in the SAR discussion, we successfully designed and synthesized in total 54 novel AXL inhibitors featuring a fused-pyrazolone carboxamide scaffold, of which up to 20 compounds including compounds **18**, **24** and **59** exhibited more potent AXL inhibitory activities and anti-BaF3/TEL-AXL cell viability potencies than the most advanced AXL inhibitor BGB324 (**1**).

Representative compound **59** with potent AXL inhibitory activities was further progressed into a docking analysis with the AXL DFG-out homology model (generated from PDB ID: 7AAY and chain B of PDB ID:7AVX). As shown in Fig. 4, the quinoline N atom bound to the residue M623 located in the hinge region *via* a key hydrogen bond interaction. The 4-aminophenol was located at the hydrophobic tunnel of AXL kinase. Moreover, the two carbonyl groups in the novel fused-pyrazolone carboxamide scaffold favorably played a DHBA role to form two hydrogen bonds with residues K567 and D690 in the allosteric pocket induced by the DFG-out conformation, respectively. More importantly, the fused-piperidine ring occupied the allosteric cavity relatively well. These results rationalized the potent AXL inhibitory activities of compound **59**.

2.4. Pharmacokinetic (PK) profiles of compounds 18, 24 and 59 in mice

Based on comprehensive consideration of the structural characteristics and their potent *in vitro* AXL inhibitory activities, compounds **18**, **24** and **59** were selected to test their PK properties in mice through oral administration and intravenous injection to provide a dosage reference for *in vivo* efficacy studies. As shown in Table 3, compounds **18**, **24** and **59** showed the similar high oral *in vivo* exposures (**18**: 15,903 ng h/mL *vs* **24**: 13,500 ng h/mL *vs* **59**: 14,800 ng h/mL) and low clearance rates (**18**: 2.05 mL/min/kg *vs* **24**: 1.70 mL/min/kg *vs* **59**: 3.86 mL/min/kg), but the oral bioavailabilities of 22.9% for **18** and 36.1% for **59** indicated that they had better gastrointestinal permeabilities than that of compound **24**. Compounds **18** and **59** also exhibited the relative higher peak concentrations (**18** C_{max}: 2970 ng/mL and **59** C_{max}: 2300 ng/mL), and compound **59** had a shorter time to peak (T_{max}: 1.0 h), indicating that it worked quickly. Overall, these
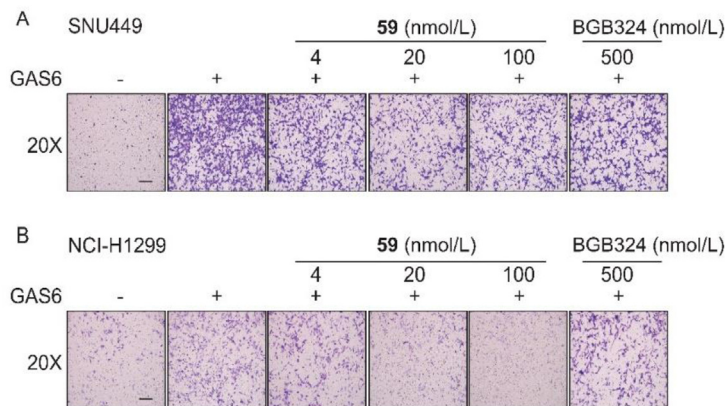
Figure 6 Compound **59** suppressed AXL-mediated tumor cell invasion and migration. (A) Effect of **59** on the GAS6-stimulated SNU449 cell invasion. Scale bars, 10 μm. (B) Effect of **59** on the GAS6-stimulated NCI-H1299 cell migration. Scale bars, 10 μm.
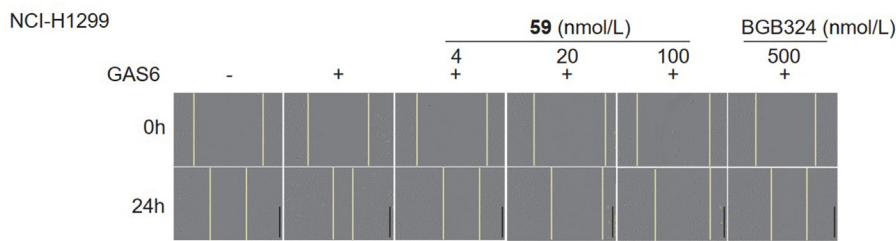
Figure 7 Compound **59** inhibited NCI-H1299 cell wound healing. NCI-H1299 cells were stimulated with 500 ng/mL GAS6 alone or co-treated with different concentrations of compound **59** or BGB324 for 24 h. Scratch healing at 0 and 24 h was observed and recorded. Representative images of triplicates were shown. Scale bars, 600 μm.

results confirmed that compounds **18** and **59** possessed relatively desired pharmacokinetic properties.

2.5. In vivo antitumor activities of compounds 18 and 59

Encouraged by the excellent *in vitro* AXL inhibitory potencies and outstanding PK properties of compounds **18** and **59**, we further established the BaF3/TEL-AXL cell-derived mouse xenograft model to investigate the *in vivo* antitumor activities (Fig. 5). Mice were orally administered with **18** and **59** at different doses of 4 and 20 mg/kg once a day for 7 consecutive days, respectively. As shown in Fig. 5A, compound **18** in both 4 mg/kg dose group and 20 mg/kg dose group exhibited significant inhibitions on tumor growth, with TGI of 89.5 % and 93.4 %, respectively. Compound **59** markedly suppressed tumor growth in a dose-dependent manner, and its antitumor efficacy at 20 mg/kg (TGI: 89.4 %) was comparable to that of BGB324 (the most advanced selective AXL inhibitor) at a dose of 50 mg/kg twice a day (TGI: 92.0 %). In addition, no significant body weight loss of tumor-bearing mice during the treatment demonstrated the well tolerance of compounds **18** and **59** (Fig. 5B).

Given that compound **59** exhibited good and dose-dependent *in vivo* anti-tumor effects, at the end of treatment, subcutaneous BaF3/TEL-AXL tumor tissues were obtained. Then, intratumoral AXL phosphorylation level was tested to validate *in vivo* AXL targeting-activity of compound **59**. The robust inhibitions of p-AXL were observed in both treatment groups (Fig. 5C). Taken together, compound **59** exhibited strong *in vitro* AXL inhibitory activities and dose-dependent *in vivo* antitumor activities, along with favorable pharmacokinetics profiles, indicating that compound **59** represented a potent AXL inhibitor and could be used for the further preclinical in-depth evaluation.

2.6. In vitro antitumor studies of compound 59 and its kinase selectivity

2.6.1. Inhibitory effects of compound 59 against GAS6/AXL-mediated cancer cell invasion, migration and wound healing

It has been widely demonstrated that AXL overactivation is closely related to tumor invasion and metastasis[5,8]. Thus, we evaluated the inhibitory effects of compound **59** against GAS6/AXL axis mediated tumor cell invasion and migration. SNU449 hepatocellular carcinoma cell line and NCI-H1299 lung cancer cell line were used for the cell invasion and migration assays, respectively. Compound **59** dose-dependently suppressed the invasion of SNU449 cells, and exhibited a significant inhibition against cell invasion at a concentration of 20 nmol/L (Fig. 6A). Similarly, a significant reduction of the migration of NCI-H1299 cells was observed after a treatment with 20 nmol/L compound **59** (Fig. 6B). We also performed wound healing assay in NCI-H1299 cells to validate the effect of compound **59** on cell motility. As shown in Fig. 7, significant acceleration of wound healing was observed upon GAS6 stimulation, while compound **59** treatment obviously inhibited GAS6-accelaerated wound healing, still showing significant scratch gaps during the same period. In addition, under the same conditions of cell motility, we found that compound **59** had no significant inhibitory effects on the cell viability of these two cell lines (Supporting Information Fig. S5), excluding that its significant inhibitions on cell migration and invasion were due to the direct cellular toxic effect. Together, compound **59** potently attenuated GAS6/AXL-mediated tumor cell invasion and migration, indicating its therapeutic potential on tumor invasion and metastasis.
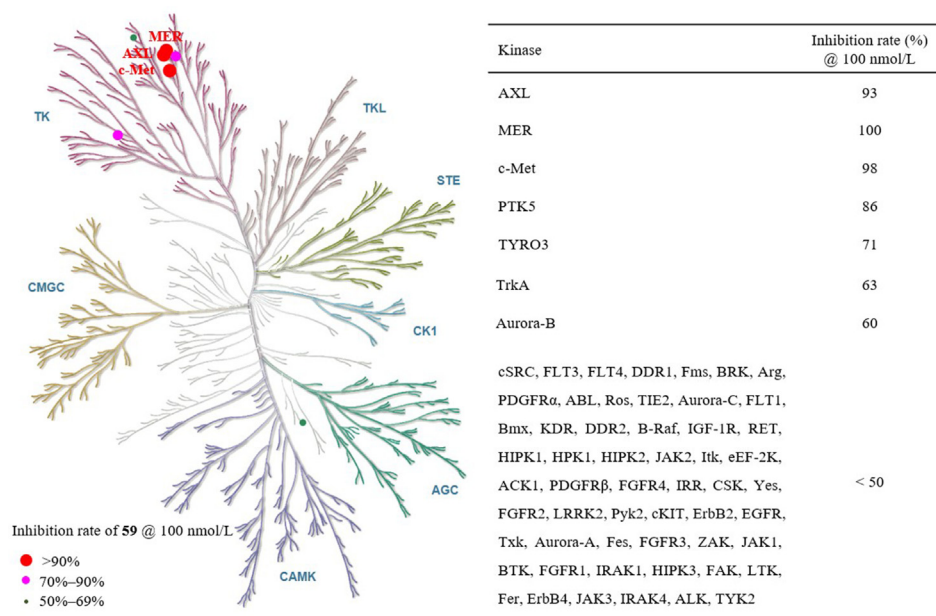
In addition, we also detected the influence of compound **59** on the E-cadherin expression, which is a canonical epithelial hallmark, and loss of E-cadherin is a hallmark of EMT[60,61]. Interestingly, GAS6 stimulation obviously downregulated E-cadherin expression, and such downregulation was significantly reversed upon compound **59** treatment (Supporting Information Fig. S6), suggesting that reversion of EMT may contribute to the inhibitory effect of compound **59** on tumor cell metastasis.

2.6.2. Inhibitory effects of compound 59 on cellular AXL signaling pathway

The inhibitory effect of compound **59** against the cellular AXL signaling pathway was investigated by Western blotting. Firstly, the classic gain of function model cell BaF3/TEL-AXL was used. As shown in Fig. 8A, compound **59** dose-dependently inhibited the phosphorylation of AXL and its key downstream signaling molecule AKT and STAT3, and showed a bit weaker inhibtion on p-ERK. We also tested the inhibitory effect of compound **59** against the ligand GAS6-stimulated AXL activation in NCI-H1299 cells. Consistently, the phosphorylation of AXL induced by GAS6 was significantly inhibited by compound **59** (Fig. 8B). Similarly, accompanied with p-AXL inhibition upon compound **59** or
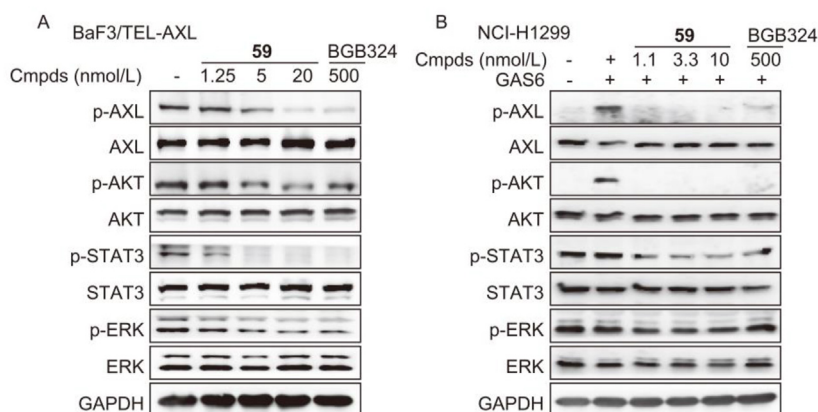
Figure 8 The effects of compound **59** on AXL signaling pathway in BaF3/TEL-AXL and NCI-H1299 cells. (A) BaF3/TEL-AXL cells were treated with compound **59** or BGB324 at indicated concentrations for 1 h, followed by immunoblotting analysis. (B) NCI-H1299 cells were deprived serum for 24 h, treated with compound **59** or BGB324 for 1 h, and then stimulated with 500 ng/mL GAS6 for 15 min, followed by immunoblotting analysis.

Kinase	Inhibition rate (%) @ 100 nmol/L
AXL	93
MER	100
c-Met	98
PTK5	86
TYRO3	71
TrkA	63
Aurora-B	60
cSRC, FLT3, FLT4, DDR1, Fms, BRK, Arg, PDGFRα, ABL, Ros, TIE2, Aurora-C, FLT1, Bmx, KDR, DDR2, B-Raf, IGF-1R, RET, HIPK1, HPK1, HIPK2, JAK2, Itk, eEF-2K, ACK1, PDGFRβ, FGFR4, IRR, CSK, Yes, FGFR2, LRRK2, Pyk2, cKIT, ErbB2, EGFR, Txk, Aurora-A, Fes, FGFR3, ZAK, JAK1, BTK, FGFR1, IRAK1, HIPK3, FAK, LTK, Fer, ErbB4, JAK3, IRAK4, ALK, TYK2	< 50

Figure 9 Kinase profile map of compound **59** drawn with KinMap[67].

BGB324 treatment, p-AKT and p-STAT3 levels were significantly inhibited, however, p-ERK was marginally inhibited upon compound **59** treatment. These results revealed that compound **59** could inhibit cellular AXL signaling. And, consistent with its inhibition on BaF3/TEL-AXL cell viability, the inhibitory potencies of compound **59** against cellular AXL signaling were much higher than that of BGB324, the most advanced selective AXL inhibitor. Interestingly, upon GAS6 stimulation in NCI-H1299 cells, acompanied with significant enhancement of p-AXL level, only p-AKT was obviously augmented while there was no obvious enhancement on p-STAT3 and p-ERK level. Our results together with other studies[62−66] suggested that the cellular downstream signaling upon AXL activation or AXL-targeting inhibiton may be different among cell lines.

2.6.3. Kinase selectivity profile of compound 59

Kinase selectivity profile of compound **59** was also performed on a panel of 62 human protein kinases highly related to oncology at a concentration of 100 nmol/L. As shown in Fig. 9, compound **59** only significantly inhibited the target kinase AXL, MER (a TAM subfamily kinase) and c-Met (an AXL homology kinase) with inhibition rates over 90 %. No obvious inhibitory effect was observed in other 55 tested kinases with inhibition rates less than 50 %. A further IC_{50} study indicated that the inhibitory activity of compound **59** against c-Met kinase with an IC_{50} of 17.3 nmol/L was weaker than that against AXL kinase with an IC_{50} of 3.5 nmol/L. In addition, we further evaluated the effect of compound **59** on c-Met-mediated cell viability in a human lung cancer cell line EBC-1 that harbors *MET* amplification, and the results demonstrated that compound **59** inhibited the viability of EBC-1 cells with an IC_{50} value of 534.9 nmol/L. Overall, compound **59** displayed a good kinase selectivity.

3. Conclusions

It's increasingly clear that inhibiting the overexpression and overactivation of AXL will represent a promising strategy for the improvement of malignant tumors therapeutic responses. By rational structure-based drug design on the hit compound **9**, we designed and synthesized in total 54 novel fused-pyrazolone carboxamide derivatives as potent and selective AXL inhibitors. Twenty compounds exhibited excellent AXL inhibitions and anticancer activities at the nanomolar level. Among them, compounds **18** and **59** displayed desirable PK profiles with excellent peak concentrations (**18** C_{max}: 2970 ng/mL and **59** C_{max}: 2300 ng/mL), *in vivo* exposures (**18** AUC: 15,903 ng h/mL and **59** AUC: 14,800 ng h/mL) and oral bioavailabilities (**18** *F*: 22.9 % and **59** *F*: 36.1 %). More importantly, both these two compounds displayed potent antitumor efficiencies in the BaF3/TEL-AXL cell-derived mouse *in vivo* model, and compound **59**, tested as the representative, showed a strong inhibitory activity against intratumoral AXL phosphorylation. Besides, compound **59** exhibited a good kinase selectivity property, and effectively blocked cellular AXL signaling in both BaF3/TEL-AXL and GAS6-stimulated NCI-H1299 cells, and significantly suppressed GAS6/AXL-mediated cancer cell invasion, migration and wound healing in a dose-dependent manner. Moreover, compound **59** significantly reversed the GAS6-stimulated downregulation of E-cadherin, the canonical epithelial hallmark, suggesting that reversion of EMT may contribute to the inhibitory effect of compound **59** on tumor cell metastasis. In conclusion, as a novel potent and selective AXL inhibitor, compound **59** possesses significant *in vitro* and *in vivo* antitumor activities, which are more potent than BGB324, as well as desirable pharmacokinetic profiles, and it could be a valuable AXL-targeted lead compound for further optimization.

4. Experimental

4.1. Chemistry

The synthetic procedures and characterization data of all target compounds and key intermediates were described in Supporting Information.

4.2.　Pharmacodynamics studies

4.2.1.　Kinase inhibition assays

The inhibitory activities of all tested compounds against AXL and c-Met kinases except for the kinase selectivity tests of compounds **9** (Supporting Information Table S1) and **59** (Supporting Information Table S2) were determined using the previously reported ELISA. A modified 4-parameter logistic model was employed to calculate IC_{50} values from the inhibition curves in at least two separate experiments. When a compound's inhibitory rate is higher than 50 % at the minimum tested concentration, its IC_{50} will be lower than the tested minimum concentration. Moreover, kinase selectivities of compound **9** (500 nmol/L) evaluated against 65 protein kinases panel and compound **59** (100 nmol/L) evaluated against 62 protein kinases panel were performed at kinase screening platform of Eurofins Discovery (France).

4.2.2.　Cell viability assays

BaF3/TEL-AXL, NCI-H1299, SNU449 and EBC-1 cells were seeded in 96-well plates with growth media at a low density, and incubated overnight. For BaF3/TEL-AXL cells, designated concentrations of BGB324 or tested compounds were added to each well, and the cells were further incubated for 48 h. For EBC-1 cells, the cells were treated with different concentrations of compound **59** or INCB28060 for 72 h. For NCI-H1299 and SNU449 cells, the cells were stimulated with 500 ng/mL GAS6 and treated with different concentrations of compound **59** or BGB324 for 24 h. Finally, the effects of tested compounds against BaF3/TEL-AXL, NCI-H1299, SNU449 and EBC-1 cells viability were determined by a cell counting kit (CCK-8) (Dojindo, Japan) assay. IC_{50} values were calculated by concentration—response curve fitting using a SoftMax pro-based four-parameter method (SoftMax® Pro Software, Version 5.4.1).

4.2.3.　Western blot analysis

BaF3/TEL-AXL cells and NCI-H1299 cells were cultured under regular growth conditions to the exponential growth phase. For BaF3/TEL-AXL cells, they were treated with the indicated dose of BGB324 or compound **59** for 1 h. For NCI-H1299 cells, they were serum-deprived for 24 h prior to treatment for 1 h with BGB324 or compound **59**, and then stimulated with GAS6 for 15 min. Then, the tested cells were lysed in $1 \times$ sodium dodecyl sulfate (SDS) sample buffer. For mice tumor tissues, they were homogenized in RIPA protein lysate by using an electric homogenizer and then determined protein content. Subsequently, the protein samples were lysed in $2 \times$ SDS sample buffer. The lysates were resolved on 10 % SDS-PAGE and transferred to nitrocellulose membranes. Proteins were probed with specific antibodies [against p-AXL (Y702), AXL, p-AKT (S473), AKT, p-STAT3(Y705), STAT3, p-ERK(Y202/204), ERK and GAPDH] (Cell Signaling Technology, USA) and a subsequent secondary horseradish peroxidase-conjugated antibody. Finally, immunoreactive proteins were detected using an enhanced chemiluminescence detection reagent (Thermo Fisher Scientific, USA).

4.2.4.　Cell migration and invasion assays

General procedures for the migration assay as follow. NCI-H1299 cells suspended in serum-free medium (1.5×10^5 cells per well) were seeded in 24-well Transwell plates (pore size, 8 μm; Corning). The bottom chambers were filled with serum-free medium supplemented with GAS6 (500 ng/mL), and designated concentrations of BGB324 or compound **59** were added to both sides of the membrane. The cultures were maintained for further 24 h, and then the non-motile cells at the top of the filter were removed using a cotton swab. The migrating cells were fixed in ethanol (90%) for 1 h and stained with crystal violet (0.1%) for 15 min at room temperature. General procedures for the invasion assay as follow. SNU449 cells were cultured in the top chambers containing matrigel-coated membrane inserts. The subsequent procedures were identical to that of the migration assay. Images were obtained using an Olympus BX51 microscope.

4.2.5.　Cell wound healing assay

NCI-H1299 cells were stimulated with 500 ng/mL GAS6 alone or co-treated with different concentrations of compound **59** or BGB324 for 24 h. Scratch healing at 0 and 24 h was observed and recorded. Images were obtained using Incucyte S3.

4.2.6.　In vivo anticancer evaluations

All procedures on animals were approved by the Institutional Animal Care and Use Committee of Shanghai Institute of Materia Medica (approval No. 2021-04-DJ-59). BaF3/TEL-AXL cells at density of $5-10 \times 10^6$ in 200 μL were implanted subcutaneously (sc) into the right flank of each nude mice and then allowed to grow to a well-developed tumor (700−800 mm³), which was further cut into 1.5 mm³ fragments and transplanted sc into the right flank of nude mice. When the tumor volume reached 50−150 mm³, the mice were randomly assigned into vehicle groups ($n = 12$) and treatment groups ($n = 6$). For the in vivo study, compounds **18** and **59** were formulated in 20 % (w/v) Labrosal-1% HPMC (pH 6.8) and BGB324 was formulated in 0.5 % HPMC, respectively. Vehicle groups were given vehicle only (20 % (w/v) Labrosal-1% HPMC (pH 6.8)), and treatment groups received BGB324 (50 mg/kg, bid), compounds **18** and **59** (4, 20 mg/kg, qd) as indicated doses via po administration. The sizes of tumors were measured twice per week using the micro-caliper, and the tumor volume (TV) was calculated as Eq. (1):

$$TV = \left(Length \times Width^2\right) / 2 \tag{1}$$

The percent (%) tumor growth inhibition (TGI) value was measured on the final day of study for drug-treated compared with vehicle-treated mice and calculated as Eq. (2):

$$TGI\ (\%) = \left\{ 1 - \left[\left(TV_{Treated\ final\ day} - TV_{Treated\ Day\ 0}\right) / \left(TV_{Vehicle\ final\ day} - TV_{Vehicle\ Day\ 0}\right) \right] \right\} \times 100 \tag{2}$$

Significant differences between treated groups vs vehicle groups ($P < 0.05$) were determined using Student's t-test. At the end of treatment, subcutaneous BaF3/TEL-AXL tumor tissues were obtained 1 h after the last dosage. Then, intratumoral AXL phosphorylation level was determined by immunoblotting analysis.

4.3. Pharmacokinetic (PK) studies

The PK properties were determined in ICR mice (6−8 weeks, 18−22 g, $n = 3$ per group). All procedures on animals were performed in accordance with the established regulations and ethical guidelines, and approved by the Institutional Animal Care and Use Committee at Shanghai Institute of Materia Medica, Chinese Academy of Sciences (approval No. 2021-07-CXY-19 and 2022-01-YY-21). For the iv groups, ICR mice were intravenously administered compounds **18** (DMSO/EtOH/PEG300/0.9 % NaCl = 5/5/40/50, *v/v/v/v*), **24** (DMSO/Tween 80/0.9 % NaCl = 5/5/90, *v/v/v*) and **59** (DMSO/Tween 80/0.9 % NaCl = 10/10/80, *v/v/v*) at doses of 5 mg/kg, respectively. The blood samples were collected at 0.083, 0.25, 0.5, 1, 2, 4, 6, 8 and 24 h after dosing. For the *po* groups, compounds **18**, **24** and **59** were treated with a solution of 20 % (*w/v*) Labrosal-1% HPMC-pH 6.8, and subsequently administered at doses of 10 mg/kg *via* oral gavage route, respectively. The blood samples were collected at 0.5, 1, 2, 4, 6, 8 and 24 h after dosing. All serum samples were obtained through common procedures of collected blood samples and stored at −80 °C until analysis, and the concentrations of the compounds in the supernatant were determined by LC−MS/MS.

4.4. Molecular modeling

Given 68.94 % sequence identities between AXL and MER kinase domains, we first aligned their sequences on https://blast.ncbi.nlm.nih.gov, and then confirmed the residues of ligand binding pockets in MER crystal structures (chain B of PDB ID: 7AVX and PDB ID: 7AAY) by Pymol software (Supporting Information Fig. S2). Moreover, Fig. S3 and Fig. S4 showed that three-dimensional conformation and ligand binding pockets of the constructed AXL DFG-out homology model were similar to that of MER crystal structures (chain B of PDB ID: 7AVX and PDB ID: 7AAY). Therefore, PDB ID: 7AAY and chain B of PDB ID: 7AVX were identified as templates. Finally, a homology modeling was performed in PyMod 3.0 on the basis of Modeller software[68].

The molecular dockings were performed on Glide module of Schrödinger software. Specifically, the constructed AXL DFG-out homology model was identified as the protein receptor, and its structure was processed by the Protein Preparation Wizard tool, including filling in missing side chains, adding hydrogens and restrained minimization. The protein grid box was generated with the center of the binding pocket by the Receptor Grid Generation tool. The ligands were processed with the LigPrep tool. Standard precision (SP) mode of Glide was applied to dock the optimized ligands into the constructed AXL DFG-out homology model with the default parameters.

Acknowledgments

Author contributions

Yu Zhou, Jing Ai, Hong Liu and Meiyu Geng conceived and designed this project. Yu Zhou and Jing Ai designed experiments and supervised data analysis. Feifei Fang, Yang Dai, Xia Peng, Jing Ai and Yu Zhou wrote the manuscript. Feifei Fang and Yang Dai analyzed the data, and together with Xia Peng, Dong Zhang and Dan Zhang drew figures and tables. Feifei Fang, Hao Wang, Yazhou Li and Chunpu Li synthesized the target compounds and key intermediates. Yang Dai, Yinchun Ji, Yangrong Zhao, Xia Peng and Danyi Wang performed *in vitro* and *in vivo* experiments of AXL inhibition and antitumor efficacy. Jiyuan Li and Chunpu Li conducted molecular docking. Feifei Fang and Xuewu Liang performed the homology modeling of AXL protein. All authors have given approval to the final version of the manuscript.

Conflicts of interest

The authors declare no competing financial interest.

Appendix A. Supporting information

Supporting data to this article can be found online at https://doi.org/10.1016/j.apsb.2023.10.002.

References

1. Varnum BC, Young C, Elliott G, Garcia A, Bartley TD, Fridell YW, et al. AXL receptor tyrosine kinase stimulated by the vitamin K-dependent protein encoded by growth-arrest-specific gene 6. *Nature* 1995;**373**:623−6.
2. Gay CM, Balaji K, Byers LA. Giving AXL the axe: targeting AXL in human malignancy. *Br J Cancer* 2017;**116**:415−23.
3. Linger RMA, Keating AK, Earp HS, Graham DK. TAM receptor tyrosine kinases: biologic functions, signaling, and potential therapeutic targeting in human cancer. *Adv Cancer Res* 2008;**100**:35−83.
4. Graham DK, DeRyckere D, Davies KD, Earp HS. The TAM family: phosphatidylserine-sensing receptor tyrosine kinases gone awry in cancer. *Nat Rev Cancer* 2014;**14**:769−85.
5. Zhu C, Wei Y, Wei X. AXL receptor tyrosine kinase as a promising anti-cancer approach: functions, molecular mechanisms and clinical applications. *Mol Cancer* 2019;**18**:153.
6. Antony J, Thiery JP, Huang RYJ. Epithelial-to-mesenchymal transition: lessons from development, insights into cancer and the potential of EMT-subtype based therapeutic intervention. *Phys Biol* 2019;**16**:041004.
7. Antony J, Huang RYJ. AXL-driven EMT state as a targetable conduit in cancer. *Cancer Res* 2017;**77**:3725−32.
8. Rankin EB, Giaccia AJ. The receptor tyrosine kinase AXL in cancer progression. *Cancers* 2016;**8**:103.
9. Valverde P, Obin MS, Taylor A. Role of GAS6/AXL signaling in lens epithelial cell proliferation and survival. *Exp Eye Res* 2004;**78**:27−37.
10. Du WT, Phinney NZ, Huang HC, Wang ZN, Westcott J, Toombs JE, et al. AXL is a key factor for cell plasticity and promotes metastasis in pancreatic cancer. *Mol Cancer Res* 2021;**19**:1412−21.
11. Tanaka M, Dykes SS, Siemann DW. Inhibition of the AXL pathway impairs breast and prostate cancer metastasis to the bones and bone remodeling. *Clin Exp Metastasis* 2021;**38**:321−35.
12. Wu XL, Ma WJ, Zhou QH, Yan HJ, Lim ZF, Huang MY, et al. AXL-GAS6 expression can predict for adverse prognosis in non-small cell lung cancer with brain metastases. *J Cancer Res Clin* 2017;**143**:1947−57.
13. Xu JC, Jia L, Ma HY, Li YP, Ma ZH, Zhao YF. AXL gene knockdown inhibits the metastasis properties of hepatocellular carcinoma *via* PI3K/AKT-PAK1 signal pathway. *Tumor Biol* 2014;**35**:3809−17.

14. Ye G, Huang M, Li Y, Ouyang J, Chen M, Wen Q, et al. The FAPα-activated prodrug Z-GP-DAVLBH inhibits the growth and pulmonary metastasis of osteosarcoma cells by suppressing the AXL pathway. *Acta Pharm Sin B* 2022;**12**:1288−304.

15. Collina F, La Sala L, Liotti F, Prevete N, La Mantia E, Chiofalo MG, et al. AXL is a novel predictive factor and therapeutic target for radioactive iodine refractory thyroid cancer. *Cancers* 2019;**11**:785.

16. Zhang S, Xu XS, Yang JX, Guo JH, Chao TF, Tong YX. The prognostic role of GAS6/AXL axis in solid malignancies: a meta-analysis and literature review. *OncoTargets Ther* 2018;**11**:509−19.

17. Liu J, Wang K, Yan ZL, Xia Y, Li J, Shi LH, et al. AXL expression stratifies patients with poor prognosis after hepatectomy for hepatocellular carcinoma. *PLoS One* 2016;**11**:e0154767.

18. Hsieh MS, Yang PW, Wong LF, Lee JM. The AXL receptor tyrosine kinase is associated with adverse prognosis and distant metastasis in esophageal squamous cell carcinoma. *Oncotarget* 2016;**7**:36956−70.

19. Hutterer M, Knyazev P, Abate A, Reschke M, Maier H, Stefanova N, et al. AXL and growth arrest-specific gene 6 are frequently overexpressed in human gliomas and predict poor prognosis in patients with glioblastoma multiforme. *Clin Cancer Res* 2008;**14**:130−8.

20. Son HY, Jeong HK. Immune evasion mechanism and AXL. *Front Oncol* 2021;**11**:756225.

21. Tanaka M, Siemann DW. GAS6/AXL signaling pathway in the tumor immune microenvironment. *Cancers* 2020;**12**:1850.

22. Rothlin CV, Ghosh S, Zuniga EI, Oldstone MBA, Lemke G. TAM receptors are pleiotropic inhibitors of the innate immune response. *Cell* 2007;**131**:1124−36.

23. Engelsen AST, Lotsberg ML, Abou Khouzam R, Thiery JP, Lorens JB, Chouaib S, et al. Dissecting the role of AXL in cancer immune escape and resistance to immune checkpoint inhibition. *Front Immunol* 2022;**13**:869676.

24. Synn CB, Kim SE, Lee HK, Kim MH, Kim JH, Lee JM, et al. SKI-G-801, an AXL kinase inhibitor, blocks metastasis through inducing antitumor immune responses and potentiates anti-PD-1 therapy in mouse cancer models. *Clin Transl Immunol* 2022;**11**:e1364.

25. Guo Z, Li Y, Zhang D, Ma J. AXL inhibition induces the antitumor immune response which can be further potentiated by PD-1 blockade in the mouse cancer models. *Oncotarget* 2017;**8**:89761−4.

26. Wu G, Ma Z, Cheng Y, Hu W, Deng C, Jiang S, et al. Targeting GAS6/TAM in cancer cells and tumor microenvironment. *Mol Cancer* 2018;**17**:20.

27. Namba K, Shien K, Takahashi Y, Torigoe H, Sato H, Yoshioka T, et al. Activation of AXL as a preclinical acquired resistance mechanism against osimertinib treatment in EGFR-mutant non-small cell lung cancer cells. *Mol Cancer Res* 2019;**17**:499−507.

28. Sen T, Tong P, Diao LX, Li LR, Fan YH, Hoff J, et al. Targeting AXL and mTOR pathway overcomes primary and acquired resistance to WEE1 inhibition in small-cell lung cancer. *Clin Cancer Res* 2017;**23**:6239−53.

29. Wang C, Jin HJ, Wang N, Fan SH, Wang YY, Zhang YR, et al. GAS6/AXL axis contributes to chemoresistance and metastasis in breast cancer through AKT/GSK-3 beta/beta-catenin signaling. *Theranostics* 2016;**6**:1205−19.

30. Scaltriti M, Elkabets M, Baselga J. Molecular pathways: AXL, a membrane receptor mediator of resistance to therapy. *Clin Cancer Res* 2016;**22**:1313−7.

31. Sun ZG, Liu JH, Zhang JM, Qian Y. Research progress of AXL inhibitors. *Curr Top Med Chem* 2019;**19**:1338−49.

32. Myers SH, Brunton VG, Unciti-Broceta A. AXL inhibitors in cancer: a medicinal chemistry perspective. *J Med Chem* 2016;**59**:3593−608.

33. Feneyrolles C, Spenlinhauer A, Guiet L, Fauvel B, Daydé-Cazals B, Warnault P, et al. AXL kinase as a key target for oncology: focus on small molecule inhibitors. *Mol Cancer Therapeut* 2014;**13**:2141−8.

34. Holland SJ, Pan A, Franci C, Hu Y, Chang B, Li W, et al. R428, a selective small molecule inhibitor of AXL kinase, blocks tumor spread and prolongs survival in models of metastatic breast cancer. *Cancer Res* 2010;**70**:1544−54.

35. Byers LA, Gold KA, Peguero JA, Johnson ML, Nieva JJ, Harb WA, et al. Ph I/II study of oral selective AXL inhibitor bemcentinib (BGB324) in combination with erlotinib in patients with advanced EGFRm NSCLC: end of trial update. *J Clin Oncol* 2021;**39**:9110.

36. Tan L, Zhang Z, Gao D, Chan S, Luo J, Tu ZC, et al. Quinolone antibiotic derivatives as new selective AXL kinase inhibitors. *Eur J Med Chem* 2019;**166**:318−27.

37. Felip E, Brunsvig P, Vinolas N, Aix SP, Costa EC, Gomez MD, et al. A phase II study of bemcentinib (BGB324), a first-in-class highly selective AXL inhibitor, with pembrolizumab in pts with advanced NSCLC: OS for stage I and preliminary stage II efficacy. *J Clin Oncol* 2019;**37**:9098.

38. Loges S, Heuser M, Chromik J, Vigil CE, Paschka P, Francesca RE, et al. First-in class selective AXL inhibitor bemcentinib (BGB324) in combination with LDAC or decitabine exerts anti-leukaemic activity in AML patients unfit for intensive chemotherapy: phase II open-label study. *J Clin Oncol* 2019;**37**:7043.

39. Traynor K. Cabozantinib approved for advanced medullary thyroid cancer. *Am J Health Syst Pharm* 2013;**70**:88.

40. Onken J, Torka R, Korsing S, Radke J, Kremenetskaia I, Nieminen M, et al. Inhibiting receptor tyrosine kinase AXL with small molecule inhibitor BMS-777607 reduces glioblastoma growth, migration, and invasion *in vitro* and *in vivo*. *Oncotarget* 2016;**7**:9876−89.

41. Chan S, Zhang Y, Wang J, Yu Q, Peng X, Zou J, et al. Discovery of 3-aminopyrazole derivatives as new potent and orally bioavailable AXL inhibitors. *J Med Chem* 2022;**65**:15374−90.

42. Zhang H, Peng X, Dai Y, Shao J, Ji Y, Sun Y, et al. Discovery of a pyrimidinedione derivative as a potent and orally bioavailable AXL inhibitor. *J Med Chem* 2021;**64**:3956−75.

43. Tan L, Zhang Z, Gao D, Luo J, Tu ZC, Li Z, et al. 4-Oxo-1,4-dihydroquinoline-3-carboxamide derivatives as new AXL kinase inhibitors. *J Med Chem* 2016;**59**:6807−25.

44. Zhan Z, Ji Y, Su H, Fang C, Peng X, Liu Q, et al. Discovery of 10*H*-benzo[*b*]pyrido[2,3-*e*][1,4]oxazine AXL inhibitors *via* structure-based drug design targeting c-Met kinase. *J Med Chem* 2022;**66**:220−34.

45. Xu D, Sun D, Wang W, Peng X, Zhan Z, Ji Y, et al. Discovery of pyrrolo[2,3-*d*]pyrimidine derivatives as potent AXL inhibitors: design, synthesis and biological evaluation. *Eur J Med Chem* 2021;**220**:113497.

46. Inoue S, Yamane Y, Tsukamoto S, Azuma H, Nagao S, Murai N, et al. Discovery of a potent and selective AXL inhibitor in preclinical model. *Bioorg Med Chem* 2021;**39**:116137.

47. Inoue S, Yamane Y, Tsukamoto S, Murai N, Azuma H, Nagao S, et al. Discovery of 5,6,7,8-tetrahydropyrido[3,4-*d*]pyrimidine derivatives as novel selective AXL inhibitors. *Bioorg Med Chem Lett* 2021;**48**:128247.

48. Okura N, Nishioka N, Yamada T, Taniguchi H, Tanimura K, Katayama Y, et al. ONO-7475, a novel AXL inhibitor, suppresses the adaptive resistance to initial EGFR-TKI treatment in EGFR-mutated non-small cell lung cancer. *Clin Cancer Res* 2020;**26**:2244−56.

49. Xu C, Han Y, Xu S, Wang R, Yue M, Tian Y, et al. Design, synthesis and biological evaluation of new AXL kinase inhibitors containing 1,3,4-oxadiazole acetamide moiety as novel linker. *Eur J Med Chem* 2020;**186**:111867.

50. Szabadkai I, Torka R, Garamvölgyi R, Baska F, Gyulavári P, Boros S, et al. Discovery of *N*-[4-(quinolin-4-yloxy)phenyl]benzenesulfonamides as novel AXL kinase inhibitors. *J Med Chem* 2018;**61**:6277−92.

51. Xi N, Wu Y, Inventors. *Bicylcic pyrazolone compounds and methods of use*. US patent WO2015164161A1; 2015.

52. Li HT, Zhu XY. Quinoline-based compounds with potential activity against drug-resistant cancers. *Curr Top Med Chem* 2021;**21**:426−37.

53. Mao YN, Soni K, Sangani C, Yao YF. An overview of privileged scaffold: quinolines and isoquinolines in medicinal chemistry as anticancer agents. *Curr Top Med Chem* 2020;**20**:2599−633.

54. Dorababu A. Report on recently (2017−20) designed quinoline-based human cancer cell growth inhibitors. *ChemistrySelect* 2020;**5**:13902−15.

55. Jain S, Chandra V, Jain PK, Pathak K, Pathak D, Vaidya A. Comprehensive review on current developments of quinoline-based anticancer agents. *Arab J Chem* 2019;**12**:4920−46.

56. Musiol R. An overview of quinoline as a privileged scaffold in cancer drug discovery. *Expet Opin Drug Discov* 2017;**12**:583−97.

57. Afzal O, Kumar S, Haider MR, Ali MR, Kumar R, Jaggi M, et al. A review on anticancer potential of bioactive heterocycle quinoline. *Eur J Med Chem* 2015;**97**:871−910.

58. Solomon VR, Lee H. Quinoline as a privileged scaffold in cancer drug discovery. *Curr Med Chem* 2011;**18**:1488−508.

59. Yao Y, Liu Z, Zhao M, Chen Z, Li P, Zhang Y, et al. Design, synthesis and pharmacological evaluation of 4-(3-chloro-4-(3-cyclopropylthi oureido)-2-fluorophenoxy)-7-methoxyquinoline-6-carboxamide (WXFL-152): a novel triple angiokinase inhibitor for cancer therapy. *Acta Pharm Sin B* 2020;**10**:1453−75.

60. Thiery JP, Acloque H, Huang RYJ, Nieto MA. Epithelial-mesenchymal transitions in development and disease. *Cell* 2009;**139**:871−90.

61. Nieto MA, Huang RY, Jackson RA, Thiery JP. EMT: 2016. *Cell* 2016;**166**:21−45.

62. Li J, Shi C, Zhou R, Han Y, Xu S, Ma H, et al. The crosstalk between AXL and YAP promotes tumor progression through STAT3 activation in head and neck squamous cell carcinoma. *Cancer Sci* 2020;**111**:3222−35.

63. Shen Y, Zhang W, Liu J, He J, Cao R, Chen X, et al. Therapeutic activity of DCC-2036, a novel tyrosine kinase inhibitor, against triple-negative breast cancer patient-derived xenografts by targeting AXL/-MET. *Int J Cancer* 2019;**144**:651−64.

64. Gomes AM, Carron EC, Mills KL, Dow AM, Gray Z, Fecca CR, et al. Stromal GAS6 promotes the progression of premalignant mammary cells. *Oncogene* 2019;**38**:2437−50.

65. Ludwig KF, Du W, Sorrelle NB, Wnuk-Lipinska K, Topalovski M, Toombs JE, et al. Small-molecule inhibition of AXL targets tumor immune suppression and enhances chemotherapy in pancreatic cancer. *Cancer Res* 2018;**78**:246−55.

66. Bárcena C, Stefanovic M, Tutusaus A, Joannas L, Menéndez A, García-Ruiz C, et al. GAS6/AXL pathway is activated in chronic liver disease and its targeting reduces fibrosis *via* hepatic stellate cell inactivation. *J Hepatol* 2015;**63**:670−8.

67. Eid S, Turk S, Volkamer A, Rippmann F, Fulle S. KinMap: a web-based tool for interactive navigation through human kinome data. *BMC Bioinf* 2017;**18**:16.

68. Janson G, Paiardini A. PyMod 3: a complete suite for structural bio-informatics in PyMOL. *Bioinformatics* 2020;**37**:1471−2.